

## Identification of crystal variants in shape-memory alloys using molecular dynamics simulations

Jo-Fan Wu<sup>1a</sup>, Chia-Wei Yang<sup>2b</sup>, Nien-Ti Tsou<sup>\*2</sup> and Chuin-Shan Chen<sup>\*\*1</sup>

<sup>1</sup>Department of Civil Engineering, National Taiwan University,  
No. 1, Sec. 4, Roosevelt Rd., Taipei 10617, Taiwan

<sup>2</sup>Department of Materials Science and Engineering, National Chiao Tung University,  
Ta Hsueh Road, HsinChu 300, Taiwan

(Received May 4, 2016, Revised June 12, 2016, Accepted July 12, 2016)

**Abstract.** Shape-memory alloys (SMA) have interesting behaviors and important mechanical properties due to the solid-solid phase transformation. These phenomena are dominated by the evolution of microstructures. In recent years, the microstructures in SMAs have been studied extensively and modeled using molecular dynamics (MD) simulations. However, it remains difficult to identify the crystal variants in the simulation results, which consist of large numbers of atoms. In the present work, a method is developed to identify the austenite phase and the monoclinic martensite crystal variants in MD results. The transformation matrix of each lattice is calculated to determine the corresponding crystal variant. Evolution of the volume fraction of the crystal variants and the microstructure in Ni-Ti SMAs under thermal and mechanical boundary conditions are examined. The method is validated by comparing MD-simulated interface normals with theoretical solutions. In addition, the results show that, in certain cases, the interatomic potential used in the current study leads to inconsistent monoclinic lattices compared with crystallographic theory. Thus, a specific modification is applied and the applicability of the potential is discussed.

**Keywords:** microstructure; molecular dynamics; Ni-Ti shape-memory alloys; phase transition

---

### 1. Introduction

Recently, many numerical models have been developed to reveal the detail of the microscopic behavior of Ni-Ti shape-memory alloys (SMA). Zhong and Zhu (2014) studied the dynamic microstructural evolution and twinning interfaces in Ni-Ti using the phase field method. Yang and Dayal (2010) also adopted this method to generate several twin microstructures. Kastner *et al.* (2011) used a molecular dynamics (MD) method to simulate the two-dimensional non-diffusive nucleation and growth processes of martensite phases giving distinct microstructures with a

---

\*Corresponding author, Assistant Professor, E-mail: [tsonienti@nctu.edu.tw](mailto:tsonienti@nctu.edu.tw)

\*\*Co-corresponding author, Professor, E-mail: [dchen@ntu.edu.tw](mailto:dchen@ntu.edu.tw)

<sup>a</sup>Master Student, E-mail: [andy@caece.net](mailto:andy@caece.net)

<sup>b</sup>Master Student, E-mail: [yang.wayne.nano03g@g2.nctu.edu.tw](mailto:yang.wayne.nano03g@g2.nctu.edu.tw)

Lennard-Jones potential. Sato *et al.* (2006) and Saitoh *et al.* (2006) revealed the microscopic mechanism of stress-induced martensitic transformation by using embedded-atom method (EAM) potentials. Several studies (Kastner *et al.* 2011, Mirzaeifar *et al.* 2014) have adopted crystallographic theory to identify martensite crystal variants in their atomistic model. However, particular crystal variants are typically assumed and, thus, the behavior of the microstructure may not be fully captured. This motivates the current study to develop a numerical procedure to identify the full set of crystal variants in the atomistic model.

Ni-Ti alloys are currently the most practical SMAs owing to their high stability, strength, and ductility and their superior thermo-mechanical performance. Hence, this study focuses on a crystal system composed of nickel and titanium atoms. In general, SMAs have two phases: the austenite and martensite phases. The former is more stable at higher temperatures while the latter is more stable at lower temperatures. The solid-solid phase transition between the austenite parent phase and the martensite phase plays a critical role in the whole process for the most important phenomena: superelasticity and the shape-memory effect. In the current study, a numerical method is developed that can effectively reveal the configuration of crystal variants in the MD simulation results. The method is then applied to study the phase transition between austenite (B2) and the monoclinic (B19') crystal system under various loading cases. The detailed microstructural evolution is revealed and the applicability of the potential used in the current work is discussed.

## 2. Theory and methodology

### 2.1 Cubic-to-monoclinic phase transition

The deformation gradient describes the local characteristics of unit cell deformation during the phase transition. A general expression for any homogeneous deformation can be written as  $\mathbf{y}=\mathbf{F}\mathbf{x}+\mathbf{c}$ , where matrix  $\mathbf{F}$  and vector  $\mathbf{c}$  are constants (Bhattacharya 2003). According to the polar decomposition theorem (Chadwick 2012), the deformation gradient  $\mathbf{F}$  can be decomposed into a pure distortion  $\mathbf{U}$  following a pure rotation  $\mathbf{Q}$ . The stretch  $\mathbf{U}$  is a positive-definite symmetric

$$\begin{aligned}
 \mathbf{U}_1 &= \begin{pmatrix} \gamma & \varepsilon & \varepsilon \\ \varepsilon & \alpha & \delta \\ \varepsilon & \delta & \alpha \end{pmatrix}, & \mathbf{U}_5 &= \begin{pmatrix} \alpha & \varepsilon & \delta \\ \varepsilon & \gamma & \varepsilon \\ \delta & \varepsilon & \alpha \end{pmatrix}, & \mathbf{U}_9 &= \begin{pmatrix} \alpha & \delta & \varepsilon \\ \delta & \alpha & \varepsilon \\ \varepsilon & \varepsilon & \gamma \end{pmatrix}, \\
 \mathbf{U}_2 &= \begin{pmatrix} \gamma & -\varepsilon & -\varepsilon \\ -\varepsilon & \alpha & \delta \\ -\varepsilon & \delta & \alpha \end{pmatrix}, & \mathbf{U}_6 &= \begin{pmatrix} \alpha & -\varepsilon & \delta \\ -\varepsilon & \gamma & -\varepsilon \\ \delta & -\varepsilon & \alpha \end{pmatrix}, & \mathbf{U}_{10} &= \begin{pmatrix} \alpha & \delta & -\varepsilon \\ \delta & \alpha & -\varepsilon \\ -\varepsilon & -\varepsilon & \gamma \end{pmatrix}, \\
 \mathbf{U}_3 &= \begin{pmatrix} \gamma & -\varepsilon & \varepsilon \\ -\varepsilon & \alpha & -\delta \\ \varepsilon & -\delta & \alpha \end{pmatrix}, & \mathbf{U}_7 &= \begin{pmatrix} \alpha & -\varepsilon & -\delta \\ -\varepsilon & \gamma & \varepsilon \\ -\delta & \varepsilon & \alpha \end{pmatrix}, & \mathbf{U}_{11} &= \begin{pmatrix} \alpha & -\delta & \varepsilon \\ -\delta & \alpha & -\varepsilon \\ \varepsilon & -\varepsilon & \gamma \end{pmatrix}, \\
 \mathbf{U}_4 &= \begin{pmatrix} \gamma & \varepsilon & -\varepsilon \\ \varepsilon & \alpha & -\delta \\ -\varepsilon & -\delta & \alpha \end{pmatrix}, & \mathbf{U}_8 &= \begin{pmatrix} \alpha & \varepsilon & -\delta \\ \varepsilon & \gamma & -\varepsilon \\ -\delta & -\varepsilon & \alpha \end{pmatrix}, & \mathbf{U}_{12} &= \begin{pmatrix} \alpha & -\delta & -\varepsilon \\ -\delta & \alpha & \varepsilon \\ -\varepsilon & \varepsilon & \gamma \end{pmatrix},
 \end{aligned} \tag{1}$$

matrix that can be determined as  $\mathbf{U} = \sqrt{\mathbf{F}^T \mathbf{F}}$ , which is also known as the transformation matrix (Hane and Shield 1999).

In order to link the continuum theory to the lattice level, the Cauchy–Born hypothesis was introduced by Eriksen (1984). Consider a crystalline solid undergoing a deformation that makes the lattice vectors  $\{\mathbf{e}_i^o(\mathbf{x})\}$  at point  $\mathbf{X}$  deform into  $\{\mathbf{e}_i(\mathbf{x})\}$ , with the relationship between these given by  $\mathbf{e}_i(\mathbf{x}) = \mathbf{F}(\mathbf{x})\mathbf{e}_i^o(\mathbf{x})$ . Thus, by examining the lattice vectors in the unit cell, one can identify the corresponding phase. Here, we take the cubic-to-monoclinic phase transition as an example. There are twelve specific transformation matrices, given by:

Where the components of the matrices ( $\alpha$ ,  $\gamma$ ,  $\delta$ ,  $\varepsilon$ ) are the material properties, and can be written in the form of the lattice parameters  $a_0$ ,  $a$ ,  $b$ ,  $c$  and  $\beta$

$$\begin{aligned} \gamma &= \frac{a(\sqrt{2}a + c \sin \beta)}{a_0 \sqrt{2a^2 + c^2 + 2\sqrt{2}ac \sin \beta}}, \quad \alpha = \frac{1}{2\sqrt{2}a_0} \left( \frac{c(c + \sqrt{2}a \sin \beta)}{\sqrt{2a^2 + c^2 + 2\sqrt{2}ac \sin \beta}} + b \right), \\ \varepsilon &= \frac{ac \cos \beta}{\sqrt{2}a_0 \sqrt{2a^2 + c^2 + 2\sqrt{2}ac \sin \beta}}, \quad \text{and } \delta = \frac{1}{2\sqrt{2}a_0} \left( \frac{c(c + \sqrt{2}a \sin \beta)}{\sqrt{2a^2 + c^2 + 2\sqrt{2}ac \sin \beta}} - b \right). \end{aligned} \quad (2)$$

These lattice parameters will be explained in detail in Sec. 2.2. The components of the transformation matrix in the monoclinic crystal system in Ni-Ti, which are obtained from experiment and the current MD simulation results, are listed in Table 1.

## 2.2 Method to identify martensite variants and austenite phase

Now consider the phase transition in Ni-Ti SMAs from the cubic to monoclinic crystal system. For the initial austenite state, it is customary to pick the tetragonal cell (marked in dashed lines in Fig. 1(a)) formed inside the four adjacent cubic cells with lattice parameter  $a_0$  (Bhattacharya 2003). After the martensitic phase transition, the tetragonal unit cell is distorted, resulting in a monoclinic unit cell with lattice parameters  $a$ ,  $b$ ,  $c$  and a non-90° angle  $\beta$  between edges  $a$  and  $c$ . It is worth noting that the monoclinic unit cell is similar to a face-centered tetragonal cell with a plane of atoms shifted from its original position, as shown in Fig. 1(b). Thus, it is necessary to describe the lattice deformation by the tetragonal cell rather than the cubic one. There are twelve types of unit cell distortion corresponding to the twelve monoclinic variants with the transformation matrices  $\mathbf{U}_m(m=1\dots 12)$  given in Eq. (1). Thus, they can serve as the standard for identification of crystal variants in MD simulations. The framework of the algorithm in the current study is illustrated in Fig. 2 and was implemented with MATLAB.

Consider the atom arrangement after energy minimization. An independent MD calculation is performed to form a pure monoclinic martensite variant. Then, the resulting position of the atoms

Table 1 Parameters of the transformation matrices in the monoclinic crystal system

Composition	$\alpha$	$\gamma$	$\delta$	$\varepsilon$	Source
Ni-49.75 at.%Ti	1.0243	0.9563	-0.058	-0.0427	(Hane and Shield 1999, Knowles and Smith 1981)
Ni-50.00 at.%Ti	1.0003	0.9978	-0.0046	-0.0238	Current work

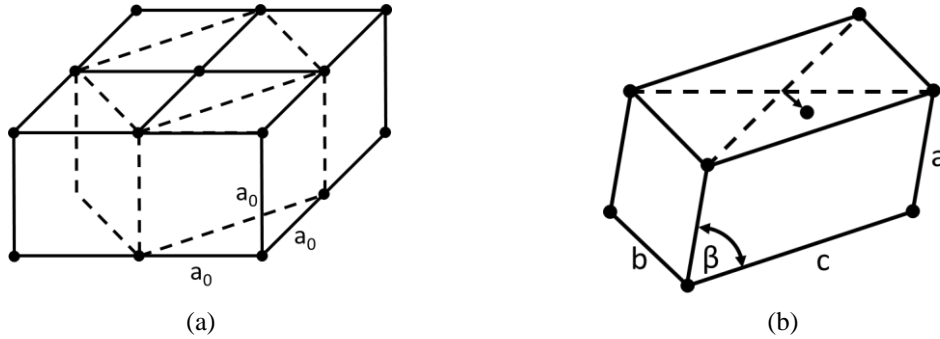


Fig. 1 The martensitic transformation in Ni-Ti alloys (only the Ti atoms are shown): (a) the cubic unit cells and a tetragonal unit cell marked with dashed lines and (b) the unit cell of the monoclinic martensite phase

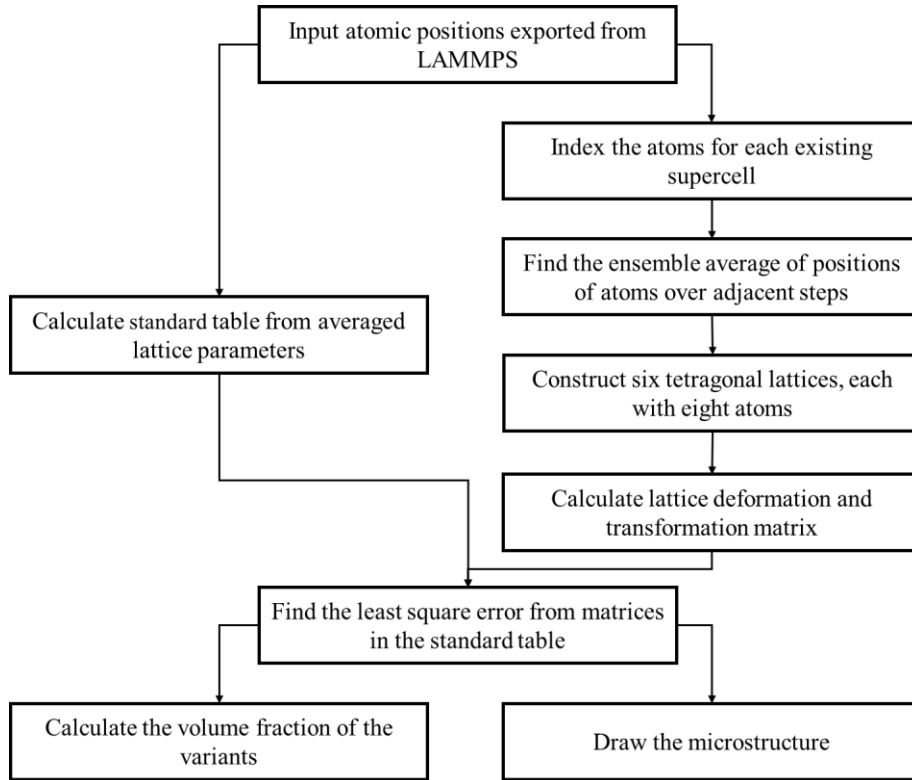


Fig. 2 Flowchart of the algorithm

can serve as the reference configuration. A set of mean lattice parameters ( $a$ ,  $b$ ,  $c$ ,  $\beta$ ) can then be determined. Their values are listed in Table and the standard table of monoclinic transformation matrices in the MD calculations can be obtained.

Now we are ready to examine the monoclinic variants in the microstructure by extracting the transformation matrix from each lattice. Here, the method proposed by Shimizu *et al.* (2007) is used with a slight modification. Consider a deformation gradient  $\mathbf{F}_i$  for each lattice  $i$  that maps

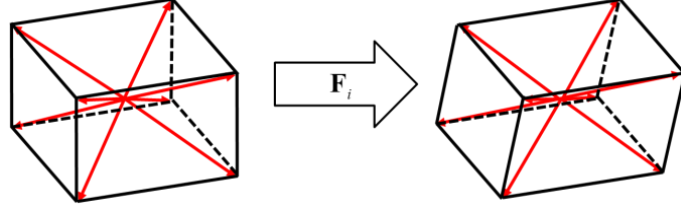


Fig. 3 Lattice deformation described by eight vectors from the center to corners of the lattice

$$\{\mathbf{d}_j^0\} \rightarrow \{\mathbf{d}_j\}, \forall j \in N_i^0, \quad (3)$$

where  $\mathbf{d}_j$  is the vector from the center of the lattice pointing to the  $j^{\text{th}}$  Ti atom that occupies one of the eight corners of the lattice  $i$  (the superscript 0 indicates the reference configuration), as illustrated in Fig. 3. The deformation gradient  $\mathbf{F}_i$  can be determined (Shimizu *et al.* 2007) by minimizing

$$\sum_{j \in N_i^0} |\mathbf{d}_j^0 \mathbf{F}_i - \mathbf{d}_j|^2 \quad (4)$$

Then, the transformation matrix  $\mathbf{U}$  can be determined. Note that the transformation matrices correspond to the cubic basis.

We are now ready to analyze the B19' monoclinic variants in the microstructure generated by MD simulations. All atoms in the simulation box are first divided into sets of super cells with eight cubic unit cells, as illustrated in Fig. 4(a). The transformation matrix of the six tetragonal unit cells colored in Fig. 4(b)-(d) in each super cell can be determined. Each transformation matrix is a possible candidate for the variants in the super cell. The error  $\sigma_m$  between each calculated transformation matrix and the standard monoclinic transformation matrices is obtained by

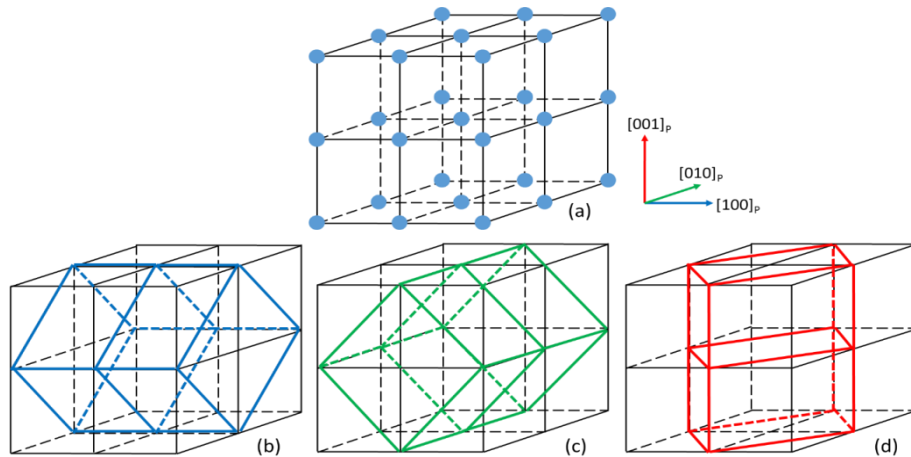


Fig. 4(a) A super cell formed by eight adjacent unit cells. Titanium atoms are shown as blue circles. Two tetragonal cells with short axes lying on (b)  $[100]_{\text{cubic}}$ , (c)  $[010]_{\text{cubic}}$ , and (d)  $[001]_{\text{cubic}}$  directions

$$\sigma_m = \sum_{j=1}^3 \sum_{k=j}^3 (\mathbf{U}_{jk}^i - \mathbf{U}_{jk}^m)^2, \forall m=1 \sim 13 \quad (5)$$

where  $i$  denotes the lattice number among the six tetragonal unit cells,  $m=1-12$  stands for the twelve standard transformation matrices and  $m=13$  indicates the non-deformed lattice, i.e., the austenite phase. The crystal variant is determined based on the tetragonal unit cell with the minimum error. Note that perturbation of atoms during the simulation is eliminated by applying the ensemble average method.

### 2.3 Compatibility equation

To validate the current method, the interfaces separating the identified crystal variants were examined using the compatibility equation. For any variant pair ( $I:J$ ) in a twinned microstructure, the compatibility equation can be written as

$$\mathbf{Q}\mathbf{U}_I - \mathbf{U}_J = \mathbf{a} \otimes \hat{\mathbf{n}}, \quad (6)$$

where  $\mathbf{a}$  is a non-zero vector and  $\hat{\mathbf{n}}$  denotes the interface normal, which can be determined by

$$\mathbf{a} = \rho \left( \sqrt{\frac{\lambda_3(1-\lambda_1)}{\lambda_3-\lambda_1}} \hat{\mathbf{e}}_1 + \kappa \sqrt{\frac{\lambda_1(1-\lambda_3)}{\lambda_3-\lambda_1}} \hat{\mathbf{e}}_3 \right), \quad (7)$$

and

$$\hat{\mathbf{n}} = \frac{\sqrt{\lambda_3} - \sqrt{\lambda_1}}{\rho \sqrt{\lambda_3 - \lambda_1}} \left( -\sqrt{1-\lambda_1} \mathbf{U}_J^T \hat{\mathbf{e}}_1 + \kappa \sqrt{\lambda_3-1} \mathbf{U}_J^T \hat{\mathbf{e}}_3 \right), \quad (8)$$

where  $\hat{\mathbf{e}}_i$  ( $i=1,2,3$ ) are the eigenvectors corresponding to the eigenvalues  $\lambda_i$  of the matrix  $\mathbf{Q}\mathbf{U}_I - \mathbf{U}_J$  and  $\rho$  is a non-zero value to ensure  $|\hat{\mathbf{n}}|=1$ . The value  $\kappa=1$  is chosen for one solution while  $\kappa=-1$  is chosen for the other. Note that any given pair of variants can either have two solutions for the twin interface normal or no solution.

## 2.4 Molecular dynamics simulations for SMAs

### 2.4.1 Interatomic potential

In this work, a Finnis-Sinclair (FS) many-body interatomic potential (Finnis and Sinclair 1984) with the EAM is adopted for describing the Ni-Ti system. This binary potential was formerly constructed by Lai and Liu (2000) and then further improved by Zhong *et al.* (2011) with modified smooth interpolations around the cutoff radius. This allows an accurate and efficient prediction of the lattice constants and energies of different phases compared to the *ab initio* calculations.

### 2.4.2 Modeling of stress-induced phase transition (model 1)

In this work, the cases of both stress- and temperature-induced phase transition are modeled by using Large-scale Atomic/Molecular Massively Parallel Simulator (LAMMPS). The settings of Model 1 for the former are detailed as follows, and those of the latter will be described in Sec.

2.4.3. A single-crystal austenite (B2) structure with Ni-Ti equiatomic composition consisting of 65,536 atoms is initialized based on the cubic parent coordinate. The entire structure contains 32 lattices (~9.6 nm long) on each side. Each single lattice is an ordered body-centered cubic (bcc) structure that contains one titanium atom and one nickel atom. The former is set at the corner and the latter at the center of the lattice. The periodic boundary condition is applied in three dimensions for bulk modeling. A random velocity seed is then chosen to generate a unique configuration of the velocity for the kinetic temperature of each atom according to the Maxwell-Boltzmann distributions.

After energy minimization using the conjugate gradient method at 0 K, the simulation box is relaxed at 150 K and zero stress with an isothermal-isobaric ensemble (NPT), at 0.5 fs/step for 100,000 time steps. Following the thermal equilibration, the temperature is set to 450 K, about 100 K higher than the austenite's final temperature  $A_f$  (~350 K), for another thermal equilibration. This two-stage thermal equilibration is to avoid the sudden temperature jump causing unstable perturbations. With the stable austenite structure, a shear deformation is applied in the  $\langle 110 \rangle$  direction to induce the cubic-to-monoclinic phase transition. The loading shear strain rate is set as  $3 \times 10^8 \text{ s}^{-1}$ , which is customarily acceptable in MD simulations, owing to the computational limitations (Zhong *et al.* 2012). The deformation continues for 1,350,000 time steps, and a 20.25% shear strain is achieved. The whole modeling process is repeated several times to demonstrate the influence of different loading directions.

#### 2.4.3 Modeling of temperature-induced phase transition (models 2 and 3)

The settings of Model 2 for temperature-induced phase transition are detailed as follows. The size of the initial structure is twice that of Model 1. The box consists of 524,288 atoms, i.e., 64 austenite lattices (~19.3 nm long) on each side. Similarly, the periodic boundary condition in three dimensions and a random velocity seed are also applied.

After energy minimization at 0 K, the simulation temperature is set to 100 K for the first thermal equilibration, and then is set to 450 K for another. Finally, the system is cooled down instantly to 100 K for equilibration. At each of the three non-zero temperature stages, the structure is relaxed at zero stress with an NPT ensemble for 100,000 time steps. It takes 50 ps for each equilibration stage, as in the previous section. The entire modeling process is repeated several times to demonstrate the influence of different velocity configurations.

Model 3 adopts the same settings as Model 2, with the difference that the temperature increases instantly from 0 K to 100 K immediately after energy minimization of the initial austenite structure. Although the process may not be physically feasible, these settings can provide numerical boundary conditions giving equal possibilities for the presence of each martensite phase in the simulation box. Thus, the competition between all twelve monoclinic martensite variants can be observed in the Model 3 simulation.

## 3. Results and discussion

### 3.1 Model validation

To validate the current method, the results of the stress-induced phase transition at 450 K with a twinning microstructure (Model 1) are compared with the theoretical solution. The model is identified by the current method, as shown in Fig. 6. Note that the six applied loading cases only

Table 2 The interface normals obtained by the compatibility equation, and identified by the current method

Shear applied	Twin pair	Theoretical solution	MD	Twin pattern
 $\begin{matrix} \uparrow [010] \\ \rightarrow [100] \end{matrix}$	(2:3)	(0.984, -0.179, 0) or (001)	(001)	Fig. 5(a)
 $\begin{matrix} \uparrow [010] \\ \rightarrow [100] \end{matrix}$	(1:4)	(001) or (0.984, -0.179, 0)	(001)	Fig. 5(b)
 $\begin{matrix} \uparrow [001] \\ \rightarrow [010] \end{matrix}$	(6:8)	(0, 0.984, -0.179) or (100)	(100)	Fig. 5(c)
 $\begin{matrix} \uparrow [001] \\ \rightarrow [010] \end{matrix}$	(5:7)	(100) or (0, 0.984, 0.179)	(100)	Fig. 5(d)
 $\begin{matrix} \uparrow [001] \\ \rightarrow [100] \end{matrix}$	(2:4)	(010) or (0.984, 0, -0.179)	(010)	Fig. 5(e)
 $\begin{matrix} \uparrow [001] \\ \rightarrow [100] \end{matrix}$	(1:3)	(0.984, 0, 0.179) or (010)	(010)	Fig. 5(f)

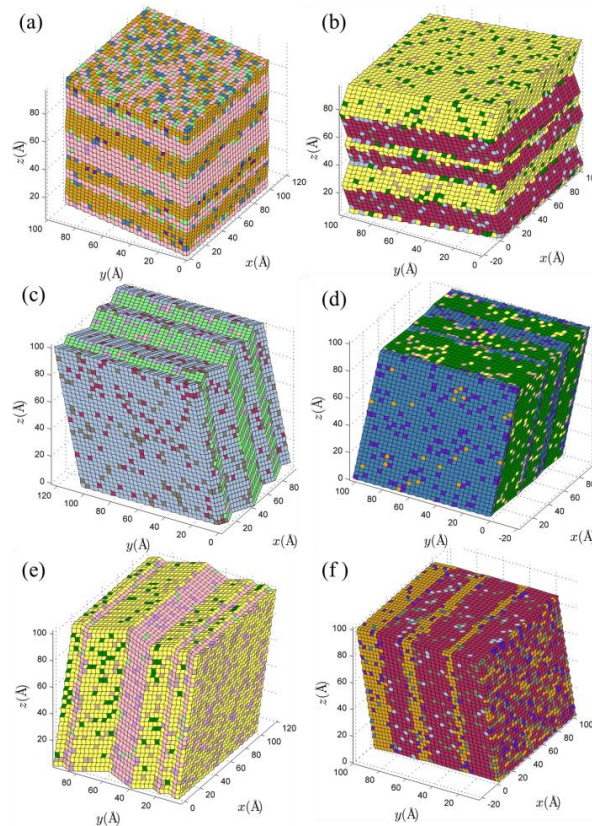


Fig. 5 Stress-induced twinning configurations at 450 K

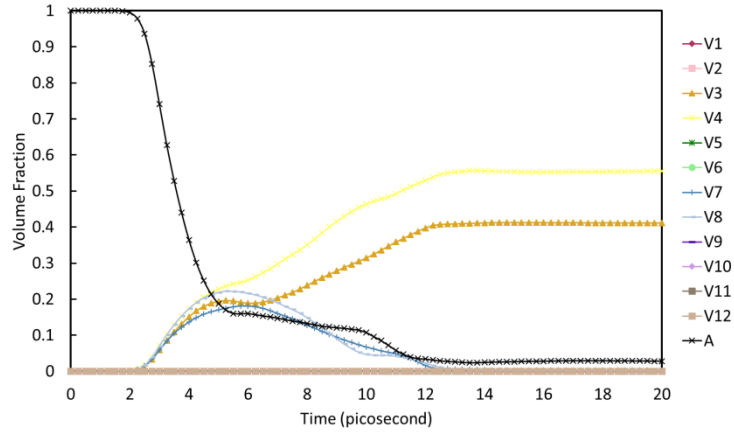


Fig. 6 The variation of the volume fraction of each variant in model 2

favor the rational solutions among the two normals and, thus, only the interfaces with a rational normal can be observed. They are validated by the compatibility equation, Eq. (6), and the results are listed in Table 2. The consistency has been ensured in each of these six cases.

### 3.2 Evolution of microstructure and volume fraction of variants

#### 3.2.1 Phase transition Induced by cooling from 450 K to 100 K

In this section, the phase transition driven by cooling from 450 K to 100 K (Model 2) is simulated. Interestingly, two types of microstructural evolution are generated. In the first type, the microstructure reaches the equilibrium state quickly within 13 ps. This can be observed in the variation of the volume fraction of all the variants present in the simulation box, as shown in Fig. 6. It is worth mentioning that the transformation matrix of the martensite lattices simulated by the FS potential in the case of the temperature-induced phase transition gives a relatively large error in Eq. (5). Here, we found that a  $45^\circ$  rotation applied on the reference axes can minimize this error, and the martensite variants can still be identified. This issue will be discussed in more detail in Sec. 3.2.3.

In Fig. 6, the vertical axis is the volume fraction of the twelve variants and the horizontal axis denotes the time in ps. The legends on the right-hand side denote the colors of variants 1-12 and the austenite lattice. At the 2<sup>nd</sup> ps, the temperature drops and induces a phase transformation, resulting in the variation of the volume fraction of variants. The instant decrease of austenite triggers the growth of variants 3, 4, 7, and 8. Four variants grow rapidly from the 2<sup>nd</sup> to the 5<sup>th</sup> ps. Then the variant pair 3 and 4 dominates at the 6<sup>th</sup> ps, and keeps growing until the equilibrium state is reached at the 13<sup>th</sup> ps. At the end of the simulation, variants 3 and 4 both have a high fraction of volume and only a small portion of austenite phase remains. The corresponding microstructural evolution is visualized in intervals of 3 ps, as shown in Fig. 7. It is worth mentioning that there are some lattices located at the twinning interfaces of variants 3 and 4, identified as the austenite phase (colored in white) in Fig. 7(f). This may be due to the symmetry of distortion across the twinning interfaces, resulting in lattices at the interface with less distortion. This causes their transformation matrix to be very close to unity, and hence, they are identified as austenite lattices.

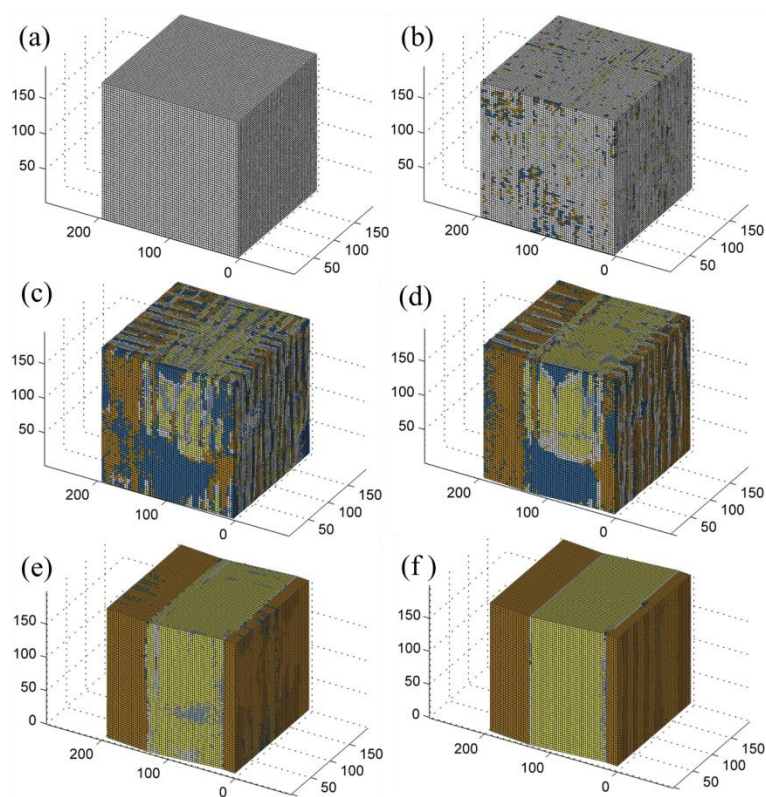


Fig. 7 Microstructural evolution in model 2 at (a) 3, (b) 6, (c) 9, (d) 12, (e) 15, and (f) 18 ps

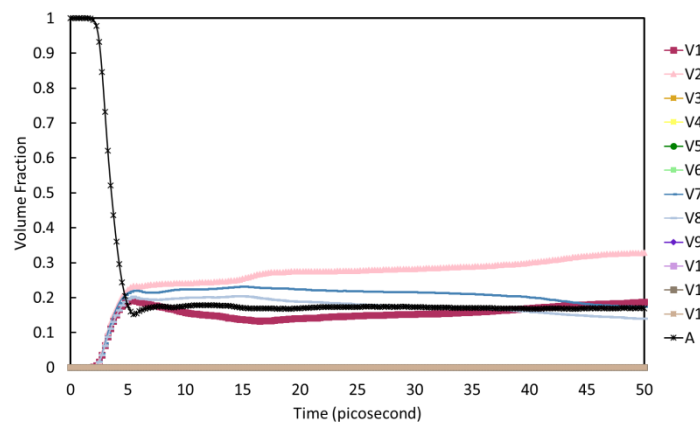


Fig. 8 The variation of volume fraction of each variant in model 2 along the alternative evolution path

The second type of results generated by Model 2 reveals an alternative path of microstructural evolution due to the choice of the random seed of the initial velocity. Fig. 8 shows the variation of the volume fraction of the variants present, and Fig. 9 shows the corresponding microstructural evolution. In the beginning of the process, two pairs of variants, 1 and 2 and 7 and 8 are nucleated and identified in the microstructure after the temperature drop from 450 K to 100 K at the 2<sup>nd</sup> ps

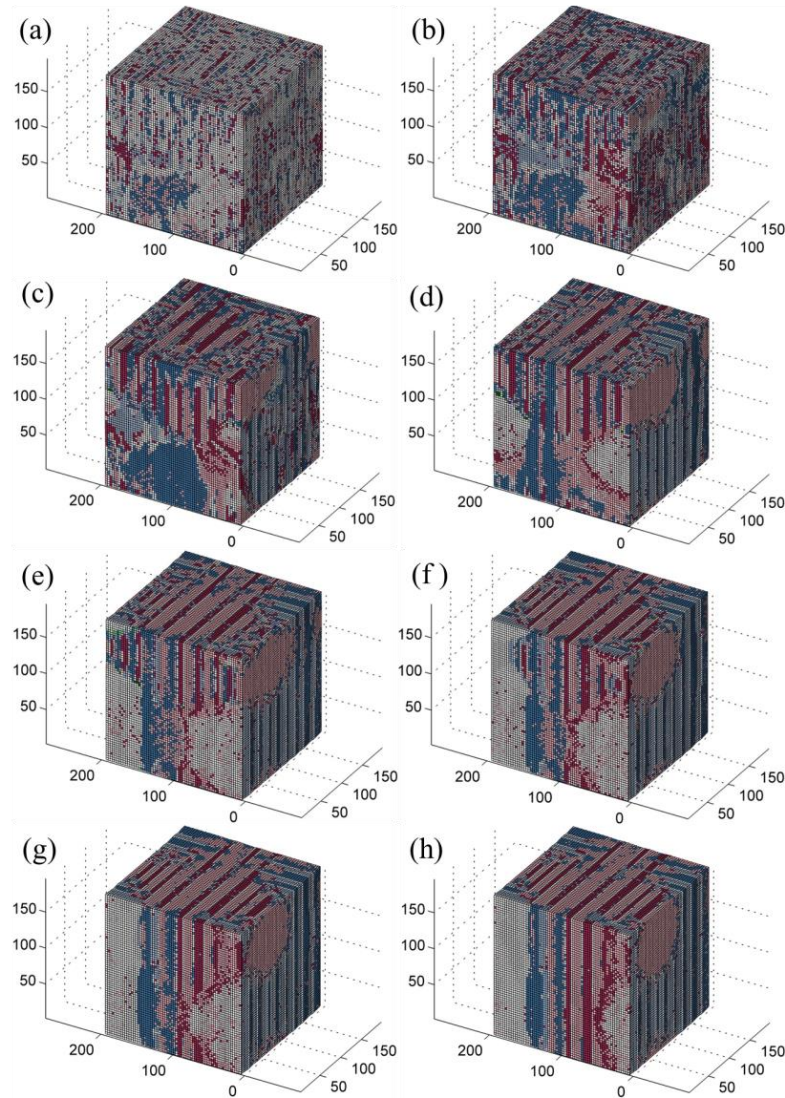


Fig. 9 Microstructural evolution in model 2 along the alternative path at (a) 5, (b) 10, (c) 15, (d) 20, (e) 25, (f) 30, (g) 40, and (h) 50 ps

(Fig. 9(a) and (b)). Then, variant 1 dissipates while variants 2, 7, and 8 grow, gradually forming the crossing twin structure, as shown in Fig. 9(c). It is remarkable that the current method can identify and illustrate the detail of the crossing twins. They have two types of interfaces: relatively sharp interfaces inside the variant pairs, and the irregular, watermark-like interfaces between the variant pairs.

Next, a new trend appears after 15 ps. The volume fraction of the variant pair 7 and 8 decreases, while variants 1 and 2 gradually increase through the rest of the simulation. However, the competition between these two pairs persists much longer compared with the previous result. Fig. 9(e)-(h) show a slow propagation of interfaces, and the volume fraction of the austenite phase remains at around 20% without significant changes.

### 3.2.2 Phase transition Induced by heating from 0 K to 100 K

In Model 3, the temperature increases instantly from 0 K to 100 K immediately after the energy minimization stage. A remarkable phenomenon is captured where the twelve monoclinic martensite variants nucleate simultaneously with a similar volume fraction at the beginning of the process, as shown in Fig. 10. This confirms that the twelve monoclinic martensite variants have equal energy states in the current simulation. A complex microstructure is formed after the perturbation of atoms given by the non-zero temperature, which breaks the metastable austenite state at 0 K, as shown in Fig. 11(a). Then, the competition between all twelve variants progresses slowly, similar to the second type of results in Model 2. A similar pattern of variations is also observed in Fig. 11(b) and (c), where the interfaces are relatively sharp inside, but irregular between the variant pairs. The propagation of these interfaces is slow, and, at the end of the simulation, martensite variants 6 and 11 and the austenite phase dominate the microstructure (Fig. 11(d)). However, equilibrium is not achieved even after the 45<sup>th</sup> ps. This result demonstrates the power of the current method, which can identify all twelve variants at the same time.

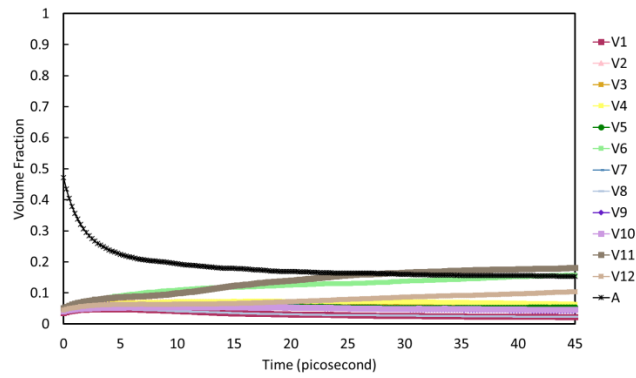


Fig. 10 The variation of volume fraction of each variant in model 3

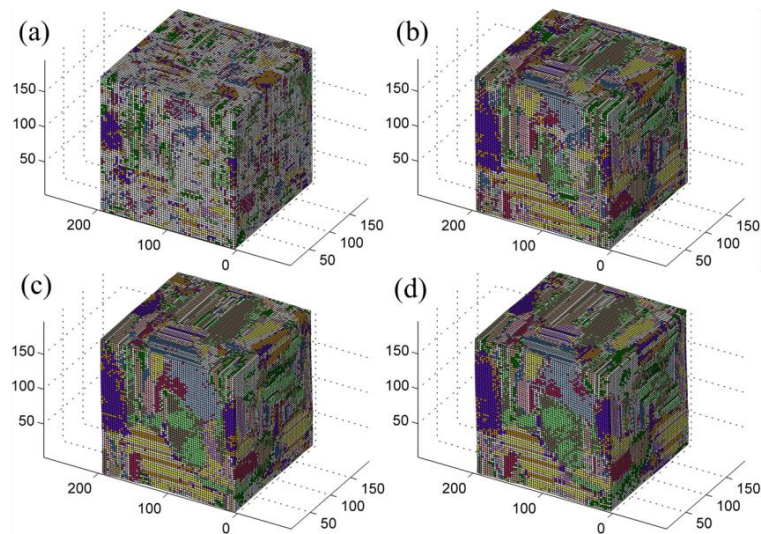


Fig. 11 Microstructural evolution in model 3 at (a) 0, (b) 15, (c) 30, and (d) 45 ps

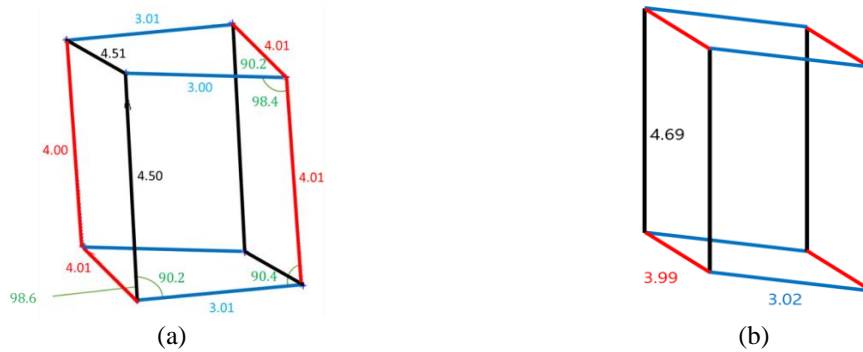


Fig. 12 Lattice structures corresponding to (a) the temperature-driven and (b) stress-induced phase transformations

### 3.2.3 The applicability of the interatomic potential

The evolution of the microstructure and volume fraction of the variants induced by stress and temperature changes were identified and analyzed in the previous sections. However, it was found that the lattice configuration of the temperature-induced monoclinic phase generated by the FS potential was inconsistent with results reported in the literature. Fig. 12(a) is an example of such a monoclinic lattice, where lines with the same color have the same length. This results in a large error in Eq. (5) during the identification of crystal variants. Here, we found that the error can be minimized if a new set of reference axes  $45^\circ$  from the original is chosen, and the variants can still be identified. In the case of the stress-induced phase transition, the resulting monoclinic lattice had good agreement with the experimental data, forming a parallelepiped structure, as shown in Fig. 12(b).

The inaccurate position of atoms in the temperature-driven phase transition may be caused by the configuration tending to seek the local energy minimum randomly when the shape of the simulation box is not strictly confined by the stress. Thus, such behavior is expected to be eliminated when stress is applied, resulting in a consistent transformation of lattices. This also indicates that the accuracy of the interatomic potential should be further improved to have better applicability for modeling the temperature-driven phase transition.

## 4. Conclusions

In the present study, a novel post-processing method for identifying the crystal variant from the results of molecular dynamics simulations based on the crystallographic and continuum theory was proposed and implemented. The method was then applied to analyze the cubic-to-monoclinic phase transformation in the Ni-Ti shape-memory alloy. For the stress-induced phase transition, the equilibrium microstructures of the six loading cases were determined. The identified interfaces were validated using the well-known compatibility equation. Next, the detailed microstructural evolution and the variation of volume fraction of the crystal variants due to different thermal boundary conditions were determined. The results showed the microstructures typically adopted an evolution path where the crystal variants grow and shrink in pairs. The results also revealed that the interatomic potential used in the current work was not sufficient to describe the stress-free

monoclinic martensite transition induced by temperature changes.

## Acknowledgments

We wish to acknowledge the support of the Ministry of Science and Technology (MOST), Taiwan, Grant No. MOST 104-2628-E-009-004-MY2. We would also like to thank the National Center for High-performance Computing (NCHC) of the National Applied Research Laboratories (NARLabs) of Taiwan for providing a computational platform.

## References

- Bhattacharya, K. (2003), "Microstructure of martensite: Why it forms and how it gives rise to the shape-memory effect", Oxford University Press.
- Chadwick, P. (2012), "Continuum mechanics: Concise theory and problems", Courier Corporation.
- Eriksen, J. (1984), "The cauchy and born hypothesis for crystals", Phase Transformations and Material Instabilities in Solids, Academic Press.
- Finnis, M.W. and Sinclair, J.E. (1984), "A simple empirical N-body potential for transition-metals", *Philos. Mag. a-Phys. Condens. Matt. Struct. Defect. Mech. Propert.*, **50**(1), 45-55.
- Hane, K.F. and Shield, T. (1999), "Microstructure in the cubic to monoclinic transition in titanium-nickel shape memory alloys", *Acta Mater.*, **47**(9), 2603-2617.
- Hane, K.F. and Shield, T.W. (1998), "Symmetry and microstructure in martensites", *Philos. Mag. A*, **78**(6), 1215-1252.
- Kastner, O., Eggeler, G., Weiss, W. and Ackland, G.J. (2011), "Molecular dynamics simulation study of microstructure evolution during cyclic martensitic transformations", *J. Mech. Phys. Sol.*, **59**(9), 1888-1908.
- Knowles, K.M. and Smith, D.A. (1981), "The crystallography of the martensitic-transformation in equiatomic nickel-titanium", *Acta Metall.*, **29**(1), 101-110.
- Lai, W.S. and Liu, B.X. (2000), "Lattice stability of some Ni-Ti alloy phases versus their chemical composition and disordering", *J. Phys. Condens. Matt.*, **12**(5), L53-L60.
- Mirzaeifar, R., Gall, K., Zhu, T., Yavari, A. and DesRoches, R. (2014), "Structural transformations in NiTi shape memory alloy nanowires", *J. Appl. Phys.*, **115**(19), 194307.
- Saitoh, K.I., Sato, T. and Shinke, N. (2006), "Atomic dynamics and energetics of martensitic transformation in nickel-titanium shape memory alloy", *Mater. Trans.*, **47**(3), 742-749.
- Sato, T., Saitoh, K.I. and Shinke, N. (2006), "Molecular dynamics study on microscopic mechanism for phase transformation of Ni-Ti alloy", *Model. Simulat. Mater. Sci. Eng.*, **14**(5), S39.
- Shimizu, F., Ogata, S. and Li, J. (2007), "Theory of shear banding in metallic glasses and molecular dynamics calculations", *Mater. Trans.*, **48**(11), 2923-2927.
- Yang, L. and Dayal, K. (2010), "Formulation of phase-field energies for microstructure in complex crystal structures", *Appl. Phys. Lett.*, **96**(8), 081916.
- Zhong, Y. and Zhu, T. (2014), "Phase-field modeling of martensitic microstructure in NiTi shape memory alloys", *Acta Mater.*, **75**, 337-347.
- Zhong, Y., Gall, K. and Zhu, T. (2011), "Atomistic study of nanotwins in NiTi shape memory alloys", *J. Appl. Phys.*, **110**(3), 033532.
- Zhong, Y., Gall, K. and Zhu, T. (2012), "Atomistic characterization of pseudoelasticity and shape memory in NiTi nanopillars", *Acta Mater.*, **60**(18), 6301-6311.